L-shell ionization in near-central collisions of heavy ions with low-*Z* atoms

M. Kavčič, M. Budnar, A. Mühleisen, P. Pelicon, Ž. Šmit, and M. Žitnik
J. Stefan Institute, P.O. Box 3000, SI-1001 Ljubljana, Slovenia

D. Castella, D. Corminboeuf, J.-Cl. Dousse, J. Hoszowska,* and P. A. Raboud
Physics Department, University of Fribourg, CH-1700 Fribourg, Switzerland

K. Tökési†
Institute of Nuclear Research of the Hungarian Academy of Sciences (ATOMKI), P.O. Box 51, H-4001, Debrecen, Hungary
(Received 24 September 1999; published 13 April 2000)

The $K\alpha$ x-ray emission spectra of Ca, Ti, Cr, and Fe targets bombarded by 2–19-MeV/amu C, O, and Ne ions were measured by means of high-resolution crystal diffractometry. The KL^N x-ray satellite lines appearing in these spectra as a result of the radiative decay of atomic states with one hole in the *K* shell and *N* in the *L* subshells could be resolved, and their relative intensities determined. The latter were corrected to account for the intra-atomic rearrangement processes preceding the *K* x-ray emission. From the values obtained the heavy ion induced *L*-shell vacancy distribution was then deduced for each collision. Significant deviations from the binomial distribution were observed. The discrepancies could be slightly diminished by assuming that the *L*-shell vacancy production is due to two uncorrelated processes: direct Coulomb ionization and target *L*-shell electron capture into the projectile *K* shell. A new KL^N vacancy yield distribution model based on statistical considerations was built, which takes into account both mechanisms of vacancy production. The average direct *L*-shell ionization probabilities per electron related to the investigated collisions were determined by fitting this distribution to the corrected experimental *L* vacancy yields, employing results of three-body classical trajectory Monte Carlo (CTMC) calculations for the electron capture probabilities. The so-obtained direct ionization probabilities were found to be somewhat smaller than the ones deduced from the standard binomial distribution, especially in low-energy collisions for which electron capture is more important. It was furthermore observed that CTMC calculations significantly overestimate the direct ionization probabilities found in the present experiment. To a smaller extent, the same holds for the geometrical model predictions, whereas theoretical results from the semiclassical approximation model were found to reproduce the experimental data better.

PACS number(s): 32.80.Hd, 32.30.Rj, 32.70.Fw

I. INTRODUCTION

Measurements of x-ray spectra emitted from target atoms after collisions with fast ions provide important information about the structure of ionized atoms, and also about the mechanisms involved in their production. If the experimental resolution is comparable to the natural widths of the emission lines, rich structures containing diagram and satellite lines can be observed in the x-ray spectrum of the target. Satellite lines correspond to photons emitted in the radiative transitions of multiply ionized atoms. Due to differences in nuclear charge screening, they are shifted to higher energies compared to the photons emitted in transitions of singly ionized atoms. The energy shift of the satellite line increases with the principal quantum number of the electron, which is active in the transition, and decreases with the principal quantum number of the additional vacancy. If the ionization of the *K* shell is accompanied by ionization in the *L* shell, KL^N satellite lines are observed on the high-energy tails of the $K\alpha$ and $K\beta$ diagram lines. Measurements of the intensity distribution of the KL^N satellite lines can be used to study the *L*-shell ionization probability in near-central collisions of ions with target atoms. This method has been well explored in the past for determination of the *L*-shell ionization probabilities of light elements induced by heavy ions [1–6]. The validity of the independent particle approximation for the description of multiple inner-shell ionization has been pointed out in most of these works. Later the satellite method was applied also to mid-*Z* [7–10] and heavy [11] elements. In these studies a detailed analysis has been performed, taking into account the change of the *K*-shell fluorescence yield due to the additional vacancies in the inner shells, and also the electron rearrangement taking place in the time interval between the collision and x-ray emission. The initial vacancy distribution can indeed be significantly different from that corresponding to the measured satellite lines. Besides direct Coulomb ionization, which is the dominant ionization mechanism in highly asymmetric collisions ($Z_{\text{projectile}} \ll Z_{\text{target}}$), other ionization processes that contribute to the production of the inner-shell vacancies were also considered in these previous works.

The satellite method has several advantages compared to measurements of the absolute *L* x-ray transition yields, which are commonly used for the study of *L*-shell ionization.

*Present address: European Synchrotron Radiation Facility (ESRF), F-38043 Grenoble, France.

†Present address: Institute for Theoretical Physics, Vienna University of Technology, A-1040 Vienna, Austria.

Since the KL^N satellite lines require the presence of a *K*-shell vacancy, such collisions can be treated as central in the *L*-shell scale. The *L*-shell ionization obtained in this manner is therefore valid only for small (near-zero) impact parameters. This offers more severe tests for the theoretical predictions than the measurements of the total cross sections, where the impact parameter dependence is smeared out by the integration process. Another advantage of this particular approach is that uncertainties of the Auger and Coster-Kronig yields enter only through the calculation of the rearrangement taking place before the x-ray emission. As a consequence of the short lifetime of the *K*-shell vacancy, these corrections are generally small so that the *L*-shell ionization probabilities are only moderately affected by the uncertainties of the Auger and Coster-Kronig yields, in contrast to the direct method.

The *L*-shell ionization study presented in this paper treats several light elements (Ca, Ti, Cr, and Fe) ionized by impact with C, O, and Ne ions in the energy range 1.5–19 Mev/amu which covers a wide domain of projectile reduced velocities ($v_{\mathrm{proj}}/v_L=\eta\sim 1-5$). The *L*-shell vacancy distributions induced by these collisions were deduced from the relative intensities of the KL^N satellites, taking into account the electron rearrangements and the changes in the fluorescence yields due to additional vacancies in the *L* shell. Our aim was to extract the single *L*-shell direct ionization probabilities from the initial vacancy distributions thus determined. This goal, however, could not be achieved straightforwardly because, besides direct ionization, electron capture into the projectile *K* shell and the shake process also contribute to the *L*-shell vacancy production. The shake contribution was determined directly from complementary measurements of the corresponding spectra produced by photoionization with an x-ray tube. This contribution was found to be negligible as compared to the direct ionization. Conversely, classical trajectory Monte Carlo (CTMC) calculations showed that at low projectile velocities ($\eta\sim 1-2$) the capture of *L* electrons of the target atom into the *K* shell of the projectile starts to compete with the direct ionization. Since the capture process cannot be directly separated from the direct ionization, a statistical model was built which describes the vacancy yield distribution, taking the two presumably uncorrelated mechanisms into account. The direct ionization probabilities were then deduced by applying this model, with incorporated CTMC capture probabilities, to the experimental vacancy distributions. The results obtained were compared with the theoretical predictions computed within the semiclassical (SCA) approximation, CTMC, and the geometrical model.

II. EXPERIMENT

The experiment was performed at the variable energy cyclotron of the Paul Scherrer Institute in Villigen, Switzerland. Metallic foils of Ca (15.5 mg/cm^2), Ti (1.36, 2.71, and 5.42 mg/cm^2), Cr (1.44, 2.88, 4.31, and 5.03 mg/cm^2), and Fe (1.57, 3.15, and 5.51 mg/cm^2) were bombarded by 34-MeV C^{2+}, 72-MeV C^{3+}, and 134-MeV C^{4+} ions, 28-MeV O^{2+}, 64-MeV O^{3+}, and 230-MeV O^{6+} ions, and 43-MeV Ne^{3+}, 160-MeV Ne^{6+}, and 380-MeV Ne^{8+} ions. Beam intensities of 20–100 nA were used. As the target foils employed in our experiment were relatively thick, the effective beam energies producing the observed x rays were calculated, taking into account the energy losses of the projectiles in the targets, the energy dependence of the *K*-shell ionization cross sections, and the absorption of the x rays on their way out from the targets.

The target x-ray emission was measured with a high-resolution von Hamos Bragg crystal spectrometer which was presented in detail in Ref. [12]. The basic elements of the spectrometer were the target-slit system which defined the x-ray source viewed by the crystal, a crystal which was cylindrically bent around an axis parallel to the dispersion plane, and a position-sensitive x-ray detector. The von Hamos spectrometer provided focusing in the nondispersive direction. For a set crystal-detector position the geometry permitted collection of x rays over an energy bandwidth limited by the detector length. To cover wider energy regions the crystal and the detector could be translated along their axes in such a way that the slit-to-crystal and crystal-to-detector distances were kept equal. The whole spectrometer was enclosed in a $180\times 62\times 24.5\,\mathrm{cm}^3$ stainless-steel chamber evacuated by a turbomolecular pump down to 10^{-7} mbar.

Emitted photons were reflected in the first order by the (200) reflecting planes of a LiF crystal. The curvature radius of the 5-cm-wide and 10-cm-high crystal was 25.4 cm, and the reflecting area was $1.3\times 10\,\mathrm{cm}^2$. Reflected photons were detected by a 27.65-mm-long and 6.9-mm-high Peltier-cooled (charged coupled device) (CCD) detector. The depletion depth of the detector was 50 μm. The detector which consisted of 1024×256 pixels, each having a size of $27\times 27\,\mu\mathrm{m}^2$, was thermoelectrically cooled to $-60\,^{\circ}\mathrm{C}$. The diffracted x rays hitting the CCD built a two-dimensional pattern on the detector plane. The horizontal axis corresponded to the energy axis of the spectrum, while the vertical dimension merely increased the collection area. The measured two-dimensional image was projected on the horizontal axis to obtain the final energy spectrum. Due to the relatively good energy resolution of the CCD detector, an energy window could be set according to the energy of the measured x rays in order to reject higher-order reflections and background events. Each image collected during the acquisition of the spectrum was filtered by this procedure. Since the 27-μm spatial resolution was not needed in our setup, we performed a software binning of four CCD columns together in order to obtain higher intensities in the position spectra.

The experimental resolution was defined mainly by the slit which defined the width of the spot viewed by the crystal. A slit width of 0.2 mm was chosen to give an experimental resolution close to the natural broadening of the observed spectral lines. The final energy resolution as determined from the photoinduced spectra was around 1.3 eV at 3.7 keV. The measured spectra were corrected for the inhomogeneous beam intensity profile on the target. No significant fluctuation of the detector efficiency along the direction of dispersion was observed. The crystal reflectivity was assumed to be constant over the surface contributing to the diffraction. This assumption was probed by measuring the Cu $K\alpha$ line in second order of reflection at different crystal positions. No

significant fluctuations in line intensity were observed [12]. In order to determine the crystal reflectivity variation as a function of the energy of the diffracted photons the $K\alpha_1$ and $K\beta_{13}$ x-ray lines of Ca, Ti, Cr, and Fe were measured. The target x-ray emission was produced by photoionization with an x-ray tube. From the comparison of the measured $I(K\alpha_1):I(K\beta_{13})$ intensity ratios with the corresponding theoretical predictions [13], the relative variation of the crystal reflectivity $[R(K\alpha_1)-R(K\beta_{13})]:R(K\alpha_1)$ was determined for each target. The reflectivity variation over the energy intervals corresponding to the measured KL^N satellite spectra was then computed from a linear interpolation of the results obtained with the $K\alpha_1$ and $K\beta_{13}$ lines. On narrow energy intervals, the variation of the crystal reflectivity is indeed linear as shown by calculations performed with the XOP code [14,15]. For two neighboring satellite lines the reflectivity correction was 1.8% for Ca, 1.1% for Ti, and 0.6% for Fe, while for Cr a negligibly small value was obtained. Although the *L*-shell ionization probabilities were found to be only slightly affected by these corrections, for each target the relative satellite yields were corrected to account for the nonconstant reflectivity of the crystal. The KL^N x-ray satellite spectra of Ca, Ti, and Cr bombarded with 28-, 64- and 230-MeV O ions are presented for illustration in Fig. 1.

We also measured the photoinduced $K\alpha$ x-ray spectra of the same elements by irradiating the targets with the bremsstrahlung of a Cr x-ray tube operated at $20\,\mathrm{kV}\times 10\,\mathrm{mA}$. The photoinduced spectra were used for the determination of the shake contribution as well as for the energy calibration of the heavy-ion-induced spectra.

III. DATA ANALYSIS

A. Fitting procedure

In a multiply ionized atom the additional vacancies reduce the nuclear charge screening. As a result the x-rays emitted by such atoms are shifted toward higher energies. As already mentioned, this shift depends on the principal quantum number of both the electron undergoing the transition, and the inner-shell spectator vacancy. If we concentrate on the KL^N satellites, the energy shift actually also depends on the subshell where the spectator vacancy is located. Considering different coupling possibilities of the total angular momenta of the open subshells, each of such KL^N satellite lines can be composed of many components. Since the energy shifts between the components are usually smaller than their natural widths, and as they are convoluted with the spectrometer response function, the KL^N satellites can only be observed as broad lines even if the experimental resolution is extremely good. Therefore the KL^N satellite spectra consist of several almost symmetric satellite lines. The latter can be fitted with single Voigt profiles which result from the convolution of the Lorentzian with the Gaussian distribution. The situation is different for the KL^0 lines. At the beam energies used in our experiment, the *L*-shell ionization is accompanied by substantial *M*-shell ionization. The degree of *M*-shell ionization at the moment of x-ray emission is even enhanced by the rearrangement processes governed mainly by the *L* Auger transitions producing additional vacancies in the *M* shell. *M*

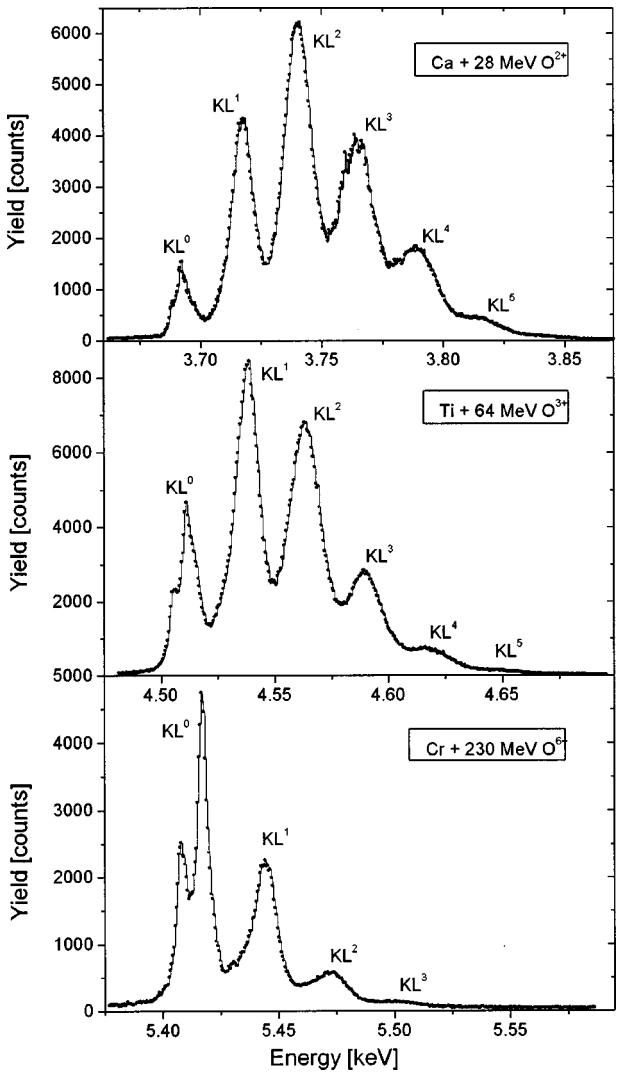

FIG. 1. Measured KL^N satellite spectra of Ca, Ti, and Cr after bombardment with 28-, 64-, and 230-MeV O ions, respectively.

satellites are much less shifted in energy than *L* satellites and, in general, they cannot be resolved from their parent diagram line. They appear in the spectra as asymmetric structures on the high energy side of the KL^0 lines. They are also present in the KL^N satellite lines, but their asymmetric contribution is smeared out due to the additional *L*-shell vacancies. In order to obtain reliable intensity distributions, the KL^0 lines were fitted in a different way. At first, we analyzed the photoinduced *K* x-ray spectra. In this case *KL* and *KM* double excitations can only result from shakeup and shakeoff processes, and are thus much weaker than in collisions involving heavy ions. Actually in the spectra produced by photoionization no asymmetry was observed on the high-energy sides of the well resolved $K\alpha_1$ and $K\alpha_2$ diagram lines (see e.g., Fig. 4). The latter could therefore be fitted with a single Voigt profile each. The energies and widths of the two Voigtians obtained from that first stage of the analysis were then kept fixed in the fits of the heavy-ion-induced KL^0 lines. The unresolved *M* satellite structures of the latter were accounted for by adding in the fit an asymmetric profile to each Voigtian. Slight asymmetry was also observed on the

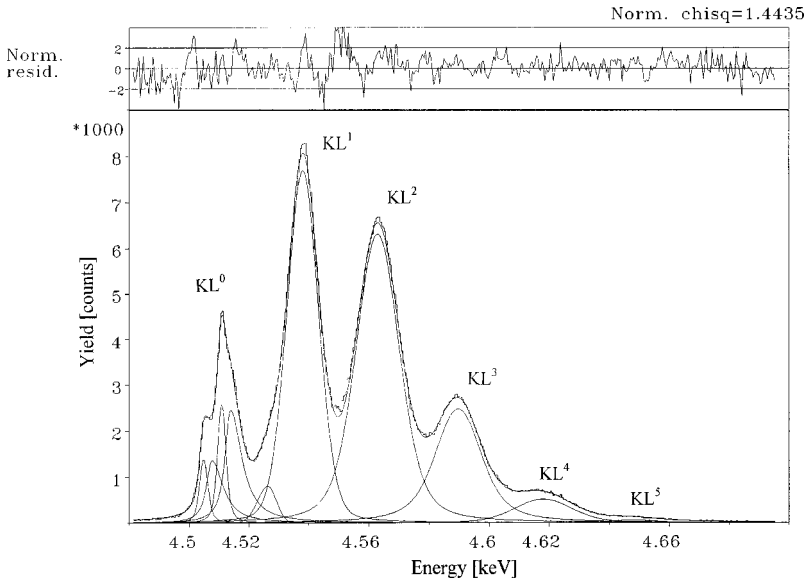

FIG. 2. KL^N satellite spectrum of Ti ionized by 64-MeV O ions. The spectrum was fitted with the model presented in the text. Voigt profiles were used for the satellite lines. The KL^0 line was fitted with two Voigt functions of fixed widths obtained from the photoinduced spectra, and two asymmetric lines describing the *M* satellites.

low-energy tail of the KL^1 line. The multiconfiguration Dirac-Fock calculation [16] revealed that the KL^1 satellite line is composed of 12 components originating from transitions between different configuration state functions. Most of them are situated within an energy gap of 5 eV, whereas two of them ($^1S_0 \rightarrow {}^1P_1$ and $^1P_1 \rightarrow {}^1S_0$), which represent less than 10% of the total KL^1 line intensity, are shifted by 10 eV to the lower energies. In the measured spectra they manifest themselves only as an asymmetry of the KL^1 line, and they were accounted for by adding an additional peak 10 eV below the Voigtian describing the main part of the KL^1 line. With this model we were able to fit the measured spectra satisfactorily and to obtain reliable intensity distributions for the KL^N lines. An example of such a fit is presented in Fig. 2. The fitting procedure was performed using the EWA dedicated program package [17].

B. Correction for electron rearrangement and satellite fluorescence yields

The KL^N satellite intensities extracted from the fitting procedure reflect the *L*-shell vacancy distribution at the moment of the x-ray emission and not the initial vacancy configuration produced in the collision. In order to obtain the initial configuration, we need to take into account the rearrangement processes that occur in the time between the ionization and the x-ray emission. These rearrangement processes are governed by *L* Auger transitions which reduce the number of initial *L*-shell vacancies. Rearrangements up to the second order were considered since the relative intensities of the *L* satellites observed in our experiment were very high. The satellite line intensities are related to the initial vacancy yields by the equations

$$X(KL^0) = [I(KL^0) + R_1^m I(KL^1) + R_1^m R_2^m I(KL^2)]\omega_{K\alpha}^{0,m}, \tag{1}$$

$$X(KL^N) = [I(KL^N)(1-R_N^m) + I(KL^{N+1})R_{N+1}^m(1-R_N^m) + I(KL^{N+2})R_{N+1}^m R_{N+2}^m]\omega_{K\alpha}^{N,m}, \tag{2}$$

where *X* denotes the x-ray line intensity, *I* the initial vacancy yield, and $\omega_{K\alpha}$ is the partial fluorescence yield for the $K\alpha$ transition. The factors R_N^m are the rearrangement factors which give the probability that the *L* shell vacancy in the atom with *N L*-shell and *m M*-shell vacancies has been promoted to an higher shell within the lifetime of the *K*-shell hole. The rearrangement factors for the *L* subshells can be written as [10]

$$R_{i,N}^m = \frac{\Gamma_{L_i}(M^m)\left(1 - \Sigma_{i<j} f_{ij}(L^N M^m)\right)}{\Gamma_{L_i}(M^m) + \Gamma_K(L^N M^m)}, \tag{3}$$

where Γ_K and Γ_{L_i} represent the total widths for the *K* shell and the L_i subshell, respectively. The Coster-Kronig transitions, which do not change the number of *L*-shell vacancies but redistribute them between the *L* subshells, are denoted by the coefficients f_{ij} in Eq. (3). The total *L*-shell rearrangement factor is given as a weighted sum of the factors for the subshells:

$$R_N^m = \sum_{i=1,2,3} w_i R_{i,N}^m . \tag{4}$$

The weighting factors in Eq. (4) depend on the *L*-subshell ionization probabilities. According to the CTMC calculations, they are almost equal (Fig. 3), so we can set the weighting factors to be $w_1 = w_2 = \frac{1}{4}$ and $w_3 = \frac{1}{2}$, according to the number of electrons in each *L* subshell.

In order to estimate the level widths for multiply ionized atoms, we need to know the relative vacancy population at the moment of x-ray emission. The *L*-subshell vacancy population is modified by the Coster-Kronig transitions between different *L* subshells. The relative L_1 and L_{23} subshell vacancy populations can be written as

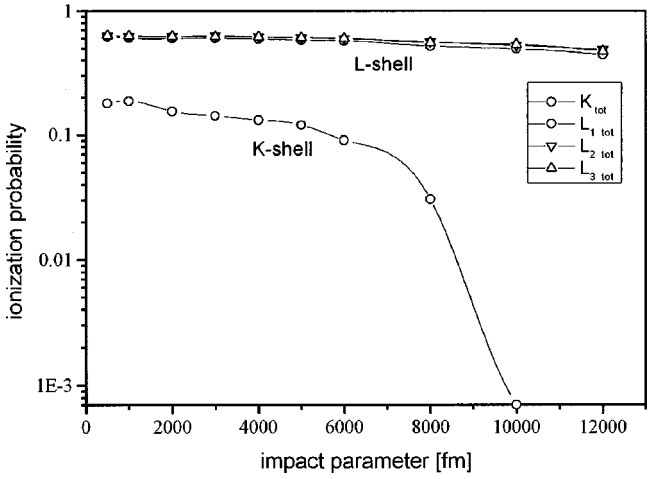

FIG. 3. Impact parameter dependence of the total ionization probabilities per electron in the *K* shell and the *L* subshells of Ca bombarded by 28-MeV O ions. The total probabilities which are the sum of the direct ionization and capture probabilities, were calculated with the CTMC model.

$$n_{L_1} = w_1\left(1 - \frac{\Gamma_{L_1} f_1}{\Gamma_K + \Gamma_{L_1} f_1}\right),$$
$$n_{L_{23}} = w_2 + w_3 + w_1 \frac{\Gamma_{L_1} f_1}{\Gamma_K + \Gamma_{L_1} f_1}, \tag{5}$$

where $f_1 = f_{12} + f_{13}$ is the Coster-Kronig yield for the L_1 subshell. For the KL^N ionized state the average number of vacancies in a subshell is given by the product of the satellite order N and the relative subshell vacancy population (Nn_{L_1} and $Nn_{L_{23}}$). Since the level widths in Eq. (5) depend on the number of vacancies in the L (and M) shell, the relative subshell vacancy population will be different for each KL^N state. We used the statistical approach proposed by Larkins [18] in order to estimate the level widths corresponding to the different KL^N states. In this approach, the width for a certain transition is proportional to the number of electrons available for that transition. For example, the $K\alpha$ radiative and the KL_1M Auger widths which both contribute to the total K shell level width for the ionized state with N L shell and m M shell vacancies can be written as

$$\Gamma^R_{K\alpha}(L^N M^m) = \frac{6 - N n_{l_{23}}}{6} \Gamma^0_{K\alpha}, \tag{6}$$

$$\Gamma^A_{KL_1M}(L^N M^m) = \frac{2 - N n_{L_1}}{2} \frac{M^{\text{total}} - m}{M^{\text{total}}} \Gamma^0_{KL_1M}. \tag{7}$$

M^{total} represents the total number of M-shell electrons of the neutral target atom. Other terms $\Gamma^R_{K\beta}, \Gamma^A_{KL_iL_i}$, $\Gamma^A_{KL_iN}, \Gamma^A_{KMM}, \ldots$, which contribute to the total K-shell level width were obtained in a similar way. As the modified level widths depend on the relative subshell vacancy populations which in turn depend on these level widths, we calculated the resulting vacancy population and K-shell level width for each KL^N state by an iterative procedure. Starting from the tabulated level widths of singly ionized atoms [19–22], we attained final subshell vacancy populations and level widths in 10–12 steps. The average number of M-shell vacancies used in this procedure was obtained by multiplying the number of M-shell electrons with the average M-shell ionization probability per electron. These ionization probabilities were calculated within the SCA [23,24] for each collision separately. The results of the iterative procedure giving the relative L-subshell vacancy populations and the K-shell level widths for the 28-MeV O-Ca collision are presented in Table I. The L-shell level widths were modified for the presence of M-shell vacancies according to the same statistical approach. The values so obtained were then employed for the calculation of the rearrangement factors as given by Eqs. (3) and (4).

TABLE I. Results of the iterative procedure described in the text giving the relative hole populations of the L subshells and the total K-shell level widths for the KL^N ionized states of Ca after bombardment with 28-MeV O ions. As a starting point the K-shell radiative widths of Scofield [19] and Auger widths of Kostroun, Chen, and Crasseman [20] were used. An average number of 1.7 M-shell holes was estimated from the SCA calculations [23,24].

	Value in eV [Ref.]	KL^1	KL^2	KL^3	KL^4	KL^5
n_{L_1}		0.071	0.061	0.051	0.041	0.032
$n_{L_{23}}$		0.929	0.939	0.949	0.959	0.968
Γ_K	0.77 [16,17]	0.593	0.471	0.365	0.273	0.196

K-shell partial fluorescence yields also depend strongly on the number of L-shell vacancies. They are then different for each satellite line, which has to be taken into account in Eqs. (1) and (2). We used the average satellite fluorescence yields quoted by Tunnel and Bhalla [25] for the elements with atomic numbers $Z = 7$, 8, 9, 10, and 14. Their results were extrapolated to our range of target atomic numbers, using a second-order polynomial. The partial fluorescence yields for the $K\alpha$ transitions were then obtained by multiplying the extrapolated values with the ratio of the $K\alpha$ transition width to the K-shell total radiative width:

$$\omega^{N,m}_{K\alpha} = \omega^N_K \frac{\Gamma^R_{K\alpha}(L^N M^m)}{\Gamma^R_K(L^N M^m)}. \tag{8}$$

In Eq. (8), ω^N_K represents the satellite fluorescence yield obtained by extrapolation of the values of Tunnel and Bhalla, while $\Gamma^R_{K\alpha}(L^N M^m)$ and $\Gamma^R_K(L^N M^m)$ are the transition and total radiative widths obtained from the above mentioned iterative procedure, respectively.

The effect of the electron rearrangement and the change of the fluorescence yields due to the additional L-shell vacancies were taken into account when evaluating the initial vacancy distributions from the measured KL^N satellite intensities. The rearrangement factors and the partial fluorescence yields corresponding to the 28-MeV O-Ca collision are presented in Table II, while the initial vacancy distribution ob-

TABLE II. Rearrangement factors and partial *K*-shell fluorescence yields for the KL^N ionized states of Ca after bombardment with 28-MeV O ions. The *K*-shell level widths were obtained from the iterative procedure described in the text. The *L*-subshell level widths and the Coster-Kronig coefficients given by Krause and Oliver [22] were modified to account for the additional *M*-shell vacancies. The partial fluorescence yields were obtained using extrapolated values of Tunnel and Bhalla [25] multiplied by the ratio of the level width for the $K\alpha$ transition and the total radiative level width of the *K* shell, both obtained from the iterative procedure.

	KL^0	KL^1	KL^2	KL^3	KL^4	KL^5
R_N^m		0.121 ± 0.029	0.145 ± 0.035	0.176 ± 0.042	0.217 ± 0.053	0.271 ± 0.065
$\omega_{K\alpha}^{N,m}$	0.148 ± 0.022	0.154 ± 0.023	0.176 ± 0.028	0.203 ± 0.030	0.225 ± 0.034	0.264 ± 0.040

tained from the relative satellite intensities is presented for the same collision in Table III. The errors of the rearrangement factors in Table II were obtained using the relative uncertainties of the *K* and L_i level widths quoted by Krause and Oliver [22] and Coster-Kronig yields quoted by Krause [21]. The relative uncertainty of the partial satellite fluorescence yields was estimated to be 15%. The errors of the vacancy yields given in Table III include those of the satellite intensities which result from the fitting procedure (computer code EWA [17]), as well as the uncertainties of the rearrangement factors and partial satellite fluorescence yields [see Eqs. (1) and (2)] quoted in Table II.

C. Ionization probabilities

In ion-atom collisions there are several mechanisms responsible for the multiple ionization of atomic inner shells. Usually the most important is the ionization due to direct Coulomb interaction between the charged particle and the bound electrons of the target atom. In more symmetric collisions ionization may also result from the capture of inner-shell electrons by the projectile. This charge exchange process decreases rapidly with projectile velocity, and is thus only important in low or intermediate velocity collisions. Shake processes represent a further possible channel for the creation of multiple-vacancy states. In this case the sudden change of the atomic potential due to the removal of a core electron results in excitation (shake-up) or ionization (shake-off) of other inner shell electrons. All these processes define the configuration of the inner-shell vacancies after the collision with an energetic ion. The main goal of the present experiment was to determine the direct ionization probabilities related to the investigated collisions. However, to avoid possible systematic errors we also need to evaluate other mechanisms that contribute to inner-shell vacancy production.

TABLE III. Observed relative satellite intensities and resulting initial vacancy yields for Ca bombarded by 28-MeV O ions. The data were corrected for the variation of the crystal reflectivity as a function of the photon energy.

	Experimental satellite yield (%)	Initial vacancy yield (%)
KL^0	4.1 ± 1.8	2.3 ± 1.8
KL^1	17.8 ± 2.2	17.9 ± 6.4
KL^2	34.6 ± 2.0	36.6 ± 9.6
KL^3	29.2 ± 4.0	29.2 ± 8.2
KL^4	11.9 ± 5.8	11.8 ± 6.4
KL^5	2.4 ± 1.5	2.3 ± 1.6

Of the processes mentioned above only the shake contribution can be determined directly. This excitation process, which is expected to be less important in our experiment than the other two, was determined from the photoinduced x-ray spectra. In Fig. 4, which represents the photoinduced $K\alpha_{1,2}$ spectrum of Ca, a very weak KL^1 shake satellite can indeed be observed on the high-energy tail of the $K\alpha_{1,2}$ line. For the other targets the shake satellites were even weaker (the shake probability varies approximately as Z^{-2}). The contribution of the shake process to the KL^N satellite spectra induced by heavy-ion impact (Fig. 1) is thus practically negligible.

If direct ionization is the main process governing multiple inner-shell ionization, then the inner shell vacancy distribution can be described, within the independent electron approximation, by a binomial distribution with the mean *L*-shell ionization probability per electron as a free parameter. The ionization cross sections for producing the KL^N ionized states can then be written as

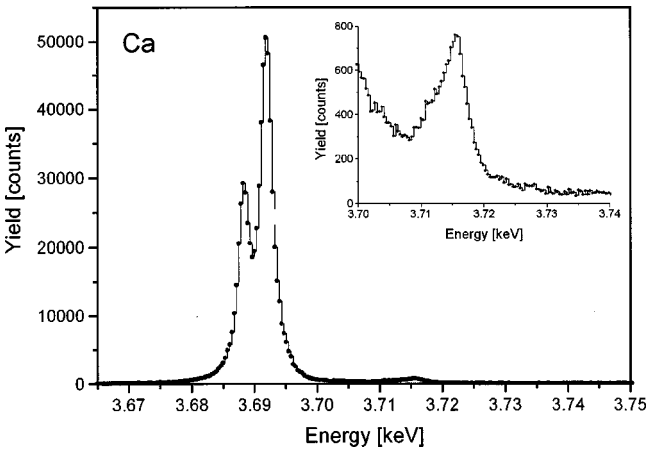

FIG. 4. Photoinduced $K\alpha$ spectrum of Ca. A weak *L* satellite line which results from shake processes is observed on the high-energy tail of the diagram line. An enlarged view of the shake satellite line is presented in the inset. The extracted satellite intensity relative to the diagram line is 0.019 ± 0.0015.

$$\sigma_{KL^N} = 2\pi \int_0^\infty 2p_K(b)[1-p_K(b)]\binom{8}{N} p_L^N(b) \times [1-p_L(b)]^{8-N} b\, db, \tag{9}$$

where b is the impact parameter, and $p_{K,L}$ are the impact parameter dependent ionization probabilities per electron for the K and L shells. Since the mean L-shell ionization probability is almost constant over the impact parameter region where the K-shell ionization probability is significant (see Fig. 3), we can simplify the above equation as

$$\sigma_{KL^N} \approx 2\pi \binom{8}{N} p_L^N(b_0)[1-p_L(b_0)]^{8-N} \times \int_0^\infty 2p_K(b)(1-p_K(b))b\, db = \binom{8}{N} p_L^N(b_0)[1-p_L(b_0)]^{8-N}\sigma_K. \tag{10}$$

The effective impact parameter b_0 is usually chosen so that the product $p_K(b_0)b_0$ is approximately maximized. Since the initial vacancy yields $I(KL^N)$ are proportional to the cross sections for producing the KL^N ionized states, the binomial distribution of Eq. (10) should reproduce the experimental KL^N vacancy distribution.

Actually we tried to fit the binomial distribution presented above to the initial vacancy distributions, and found that the experimental distributions were systematically narrower than the binomial one (see Fig. 5). Similar discrepancies were already observed for medium Z elements [8]. A possible reason for these deviations may reside in the electron capture process which was neglected in the direct ionization model leading to the binomial distribution. We calculated the probabilities for the capture of a L-shell electron into the K shell of the projectile with the three-body classical trajectory Monte Carlo model. It was found that in the lower part of the reduced velocity region covered by our experiment (i.e., in the region around $\eta \approx 1$), the electron capture (EC) probability is comparable to the direct ionization (DI) probability. This means that we cannot expect reliable results by fitting the experimental yields with the binomial distribution presented in Eq. (10) because the latter does not consider the electron capture process.

We thus tried to include the EC contribution in our calculations by describing the capture of the L-shell electrons by the projectile with a statistical model in which the target atom electrons were assumed to be independent. In this model we took into account only the capture into the projectile K shell, which is the dominant one. A similar statistical model describing the capture of target L electrons in the K shell of bare projectiles was presented by Rymuza *et al.* in Ref. [8]. The three terms occurring in this model describe the probabilities for capturing 0, 1, or 2 out of l electrons available in the L shell. We expanded this model to include the situation where only one empty state in the K shell of the projectile is available for the capture of the L-shell electrons. The situations where one or both states in the K shell of the projectile are available for capture were distinguished in the

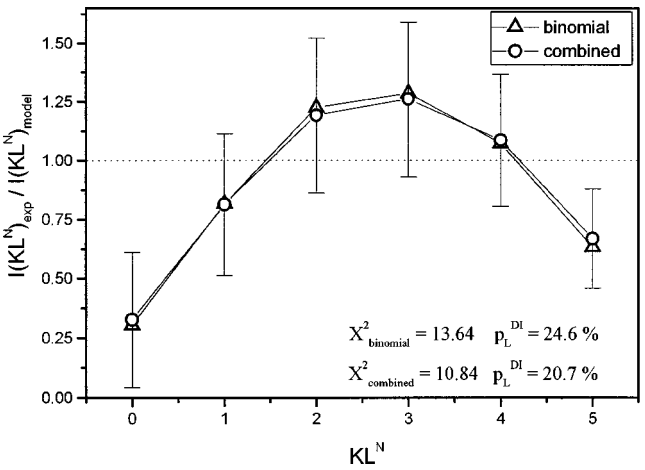

FIG. 5. Ratio of the experimental and model vacancy yields created in collisions of 43-MeV Ne ions with an Fe target. Error bars were calculated by taking into account the uncertainties of the fitted KL^N satellite yields and the uncertainties of the rearrangement factors and satellite fluorescence yields. The model yields were obtained by fitting the binomial [Eq. (10)] or the new distribution [Eq. (21)] to the experimental vacancy yield distribution. The direct ionization probability was left free in the fitting procedure. Fitting with model (21) yields $p_L^{\mathrm{DI}} = 0.196 \pm 0.009$, while the binomial model yields a higher value $p_L^{\mathrm{DI}} = 0.246 \pm 0.008$. The CTMC L-shell electron capture probability used in the combined model [Eq. (21)] was 0.293, and the ratio of the single K-shell electron direct ionization and capture cross section was 0.0134. The charge fractions of the Ne ions were $cf^{Z^+} = 0.25$, $cf^{(Z-1)^+} = 0.5$, and $cf^{Z \leqslant (Z-2)^+} = 0.25$.

new distribution by adding the parameters F_1 and F_2 which can be set to 1 or 0 alternately. When only a single K-shell state is available, the parameters are set to $F_1 = 1$, $F_2 = 0$. When the K shell is empty, the parameters are set to $F_1 = 0$ and $F_2 = 1$. Using the variable $q = [1 - p_L^{\mathrm{EC}}(b)]$, where $p_{\mathrm{EC}}^L(b)$ is the impact parameter dependent capture probability per single L-shell electron, the probability for capturing 0, 1, or 2 out of l available electrons in the L shell of the target atom in an ionic collision at an impact parameter b is given by (a) for l even,

$$P_L^{\mathrm{EC}}(b,0,l,F_1,F_2) = F_1 q^{l/2} + F_2 q^l, \tag{11}$$

$$P_L^{\mathrm{EC}}(b,1,l,F_1,F_2) = F_1(1-q^{l/2}) + F_2(2(1-q^{l/2})q^{l/2}), \tag{12}$$

$$P_L^{\mathrm{EC}}(b,2,l,F_1,F_2) = F_2(1-q^{l/2})^2, \tag{13}$$

and, for (b) l odd,

$$P_L^{\mathrm{EC}}(b,0,l,F_1,F_2) = F_1 \frac{1}{2}(q^{(l+1)/2} + q^{(l-1)/2}) + F_2 q^l, \tag{14}$$

$$P_L^{\mathrm{EC}}(b,1,l,F_1,F_2) = F_1 \tfrac{1}{2}[(1-q^{(l+1)/2}) + (1-q^{(l-1)/2})] + F_2[(1-q^{(l-1)/2})q^{(l+1)/2} + q^{(l-1)/2}(1-q^{(l+1)/2})], \tag{15}$$

$$P_L^{\mathrm{EC}}(b,2,l,F_1,F_2)=F_2(1-q^{(l-1)/2})(1-q^{(l+1)/2}). \tag{16}$$

The separation of the terms for even and odd numbers of L-shell electrons available for capture comes from the fact that for each target electron with its definite spin projection only the K-shell state, with the same spin projection value is available (spin-flip effects can be neglected in collisions with velocity $v \ll c$). Assuming that the L-shell vacancy production results from two subsequent uncorrelated processes, the probability for creating N L shell vacancies in an ion-atom collision at a certain impact parameter b can be written in a two step model (direct ionization is followed by capture, or vice versa) [8],

$$\begin{aligned}P_L^N(b,F_1,F_2)=&\tfrac{1}{2}[P_L^{\mathrm{EC}}(b,0,8,F_1,F_2)P_L^{\mathrm{DI}}(b,N,8)\\&+P_L^{\mathrm{EC}}(b,1,8,F_1,F_2)P_L^{\mathrm{DI}}(b,N-1,7)\\&+P_L^{\mathrm{EC}}(b,2,8,F_1,F_2)P_L^{\mathrm{DI}}(b,N-2,6)]\\&+\tfrac{1}{2}[P_L^{\mathrm{DI}}(b,N-2,8)P_L^{\mathrm{EC}}(b,2,10-N,F_1,F_2)\\&+P_L^{\mathrm{DI}}(b,N-1,8)P_L^{\mathrm{EC}}(b,1,9-N,F_1,F_2)\\&+P_L^{\mathrm{DI}}(b,N,8)P_L^{\mathrm{EC}}(b,0,8-N,F_1,F_2)],\end{aligned} \tag{17}$$

where $P^{\mathrm{DI}}(b,N,l)$ which is the probability for the direct ionization of N out of l electrons available in the L shell can be described with the binomial distribution

$$P_L^{\mathrm{DI}}(b,N,l)=\binom{l}{N}p_L^N(b)[1-p_L(b)]^{1-N}. \tag{18}$$

The KL^N vacancy yields are proportional to the ionization cross section

$$\begin{aligned}I(KL^N)&\propto\int_0^\infty P_K(b)P_L^N(b,F_1,F_2)b\,db\\&\approx P_L^N(b_0,F_1,F_2)\int_0^\infty P_K(b)b\,db.\end{aligned} \tag{19}$$

If incompletely bare projectiles are also considered, we can rewrite the KL^N vacancy yields in the following form:

$$\begin{aligned}I(KL^N)=C_{\mathrm{norm}}\Bigg\{&cf^{Z^+}\Bigg[P_L^N(b_0,F_1=0,F_2=1)\int_0^\infty P_K^{\mathrm{DI}}(b)b\,db\\&+P_L^N(b_0,F_1=1,F_2=0)\int_0^\infty P_K^{\mathrm{EC}}(b)b\,db\Bigg]\\&+cf^{(Z-1)^+}\Bigg[P_L^N(b_0,F_1=1,F_2=0)\int_0^\infty P_K^{\mathrm{DI}}(b)b\,db\\&+P_L^{\mathrm{DI}}(b_0,N,8)\int_0^\infty P_K^{\mathrm{EC}}(b)b\,db\Bigg]\\&+cf^{Z\leqslant(Z-2)^+}\Bigg[P_L^{\mathrm{DI}}(b_0,N,8)\int_0^\infty P_K^{\mathrm{DI}}(b)b\,db\Bigg]\Bigg\}.\end{aligned} \tag{20}$$

This equation can be given in a slightly different form:

$$\begin{aligned}I(KL^N)=C_{\mathrm{norm}}\{&\sigma_K^{\mathrm{DI}}[cf^{Z^+}P_L^N(b_0,F_1=0,F_2=1)\\&+cf^{(Z-1)^+}P_L^N(b_0,F_1\\&=1,F_2=0)+cf^{Z\leqslant(Z-2)^+}P_L^{\mathrm{DI}}(b_0,N,8)]\\&+\sigma_K^{\mathrm{EC}}[cf^{Z^+}P_L^N(b_0,F_1=1,F_2=0)\\&+cf^{(Z-1)^+}P_L^{\mathrm{DI}}(b_0,N,8)]\}.\end{aligned} \tag{21}$$

In Eq. (21), cf^{Z^+}, $cf^{(Z-1)^+}$, and $cf^{Z\leqslant(Z-2)^+}$ are the fractions of projectiles with charges Z^+, $(Z-1)^+$, and $Z\leqslant(Z-2)^+$, respectively, and C_{norm} is a normalization constant. When ions are traveling through a medium a charge equilibration is attained and the charge distribution becomes independent of the initial charge state of the ions. The equilibrium charge distribution is characteristic of the energy of the projectiles. In our case, except for 28 and 64-MeV O ions, 34-MeV C ions, and 43-MeV Ne ions, all other projectiles were assumed to be completely bare (i.e., $cf^{Z^+}=1$ and $cf^{(Z-1)^+}=cf^{Z\leqslant(Z-2)^+}=0$). For the four incompletely stripped ion beams, the charge fractions were estimated from the data obtained in Ref.[26].

In order to evaluate the $I(KL^N)$ yields given by Eq. (21), the cross sections σ_K^{DI} and σ_K^{EC} have to be known. Actually as only the relative yields are needed, it is sufficient to determine the ratios $\sigma_K^{\mathrm{DI}}/\sigma_K^{\mathrm{EC}}$. These cross-section ratios and the EC probabilities entering relation (21) were calculated within the three-body CTMC model. The K-shell EC cross sections for projectiles with the charge $(Z-1)^+$ were assumed to be half of those for bare projectiles. Furthermore, the K- and L-shell direct ionization probabilities were supposed to be nearly equal for all three charge states of the projectiles, so all values were calculated for bare projectiles. Both the EC and DI probabilities were calculated at an effective impact parameter b_0 which was set to 4000 fm.

In the case of 28-MeV O and 43-MeV Ne ions, where $cf^{Z\leqslant(Z-2)^+}>0$ (for all other ion beams the fraction of two-electron ions in the target is negligible) we have to consider the possible presence of the $1s2s$ metastable state in the two-electron ion-beam component. As the lifetime of this long-lived $1s2s$ state is comprised between 10^{-2} and 10^{-4} sec for O and Ne ions [27–29], two-electron ions in the $1s2s$ state can indeed capture one electron from the target atom, which was not considered in Eq. (21). The size of this effect was estimated by adding in Eq. (21) the factor $R_{1s2s}(cf^{Z\leqslant(Z-2)^+})$ to the factor $cf^{(Z-1)^+}$ and subtracting it from the factor $cf^{Z\leqslant(Z-2)^+}$. This model refinement, however, did not result in significant changes of our results since excited ion fractions R_{1s2s} as large as 40% were found to modify the final P_L^{DI} values by only ~1%. Therefore, the effect on the final ionization probabilities of the $1s2s$ metastable state in the two-electron ion beam component was not considered.

TABLE IV. *L*-shell direct ionization probabilities per electron (p_L^{DI}) obtained from fitting the model distribution (21) to the KL^N vacancy distribution. The quoted errors are due to the least-squares fitting procedure [34], taking into account uncertainties of the KL^N vacancy yields. The single *L*-shell electron capture probabilities (p_L^{EC}) and the ratio of the single *K*-shell direct ionization to capture cross sections $\sigma_K^{\mathrm{DI}}/\sigma_K^{\mathrm{EC}}$, both obtained from CTMC calculations, are also tabulated.

Target	Ions	E_0 (MeV)	$E_{\mathrm{effective}}$ (MeV)	$(\sigma_K^{\mathrm{DI}}/\sigma_K^{\mathrm{EC}})_{\mathrm{CTMC}}$	$(P_L^{\mathrm{EC}})_{\mathrm{CTMC}}$ (%)	P_L^{DI} (%)
Ca	O	28	24.5	0.025	26.2	27.5±1.4
Ca	O	230	224.0	2.67	0.35	8.1±0.8
Ti	O	64	60.0	0.19	8.8	17.8±1.3
Cr	O	64	59.7	0.14	9.8	15.8±1.0
Cr	O	230	226.7	1.64	0.6	7.9±0.6
Fe	O	28	25.3	0.012	20.4	17.8±1.2
Fe	O	230	226.1	1.26	0.8	6.2±0.6
Ca	C	34	29.4	0.16	8.6	18.3±0.9
Ca	C	72	65.9	0.64	1.9	11.2±0.7
Ca	C	134	129.8	2.43	0.35	6.5±0.5
Ti	C	34	32.5	0.14	7.9	16.6±0.9
Ti	C	72	70.1	0.58	2.0	9.4±0.7
Cr	C	134	131.7	1.38	0.6	5.0±0.4
Fe	C	34	32.2	0.076	8.7	13.9±1.0
Ca	Ne	380	372.5	5.24	0.2	10.3±0.9
Ti	Ne	43	39.5	0.026	32.0	27.4±1.2
Ti	Ne	380	376.0	3.60	0.35	9.6±0.7
Cr	Ne	160	152.2	0.20	4.3	17.5±1.4
Cr	Ne	380	376.0	2.49	0.4	8.2±0.6
Fe	Ne	43	39.0	0.013	29.3	20.7±0.8
Fe	Ne	160	155.0	0.32	4.7	12.8±0.7

IV. RESULTS AND DISCUSSION

For all measured collisions we fitted the experimental vacancy yields to distribution (21), which combines both the direct ionization and capture of target *L*-shell electrons into the *K* shell of the projectile. The single free fitting parameter was the average *L*-shell direct ionization probability per electron, since the *K*-shell ionization and electron capture cross sections and the probability for capturing a single *L*-shell electron were calculated within the CTMC approach, as mentioned above. We also tried to fit the experimental vacancy yields to distribution (21) by letting both parameters (p_L^{DI} and p_L^{EC}) be free. Such a fit better reproduced the experimental yields, but the final capture probabilities were overestimated significantly. Since both parameters are correlated this brought down the direct ionization probabilities. Therefore, we decided to use the capture probabilities calculated within the CTMC approach, and keep them fixed during the fitting procedure. This way the experimental yields could not be totally reproduced, but the differences were slightly diminished compared to the standard binomial distribution. The three particles used in the CTMC calculations were the bare projectile, an active atomic electron, and the remaining ion. For the description of the interaction between them, a potential model based on Hartree-Fock calculations as developed by Green [30] was used. These three-body, three-dimensional CTMC calculations were performed as described in Refs. [31,32]. The initial parameters were the same as those developed by Reinhold and Falcon [33]. They were chosen randomly at relatively large internuclear separations, where the interaction between the projectile and the target atom is negligible. The initial conditions were set from the ensemble, which is constrained to an initial binding energy of the *L*-shell target electron. For the given initial parameters, Newton's equations of motion were integrated with respect to time as independent variable by the standard Runge-Kutta method, until large separations of the colliding particles were attained. For each investigated collision, 20 000 individual trajectories were calculated.

In Fig. 5 we see the results of the fitting procedure for the case of Fe ionized by 43-MeV Ne ions. Using model (21), which combines the capture and direct ionization processes, the χ^2 of the fit was reduced by 20% as compared to the fit using the binomial distribution. It has to be noted that the direct ionization probability obtained from this fit is significantly smaller (by 16%) than that obtained from the model using the binomial distribution. As anticipated, nonconsideration of the EC process would lead to systematic errors in the direct ionization probabilities. In particular, in the low projectile velocity region, where the capture of *L*-shell electrons is highly probable, the direct ionization probabilities would be markedly overestimated by fitting the binomial distribution to the experimental values. Moreover, for high velocity collisions, where capture is almost negligible, the combined model yields results practically equal to the binomial ones.

The direct ionization probabilities deduced from the measured data for an effective impact parameter $b_0 = 4000$ fm are presented in Table IV together with the CTMC predictions for electron capture. The quoted errors are due to the least-squares fitting procedure [34] taking into account uncertainties of the KL^N vacancy yields. It will be shown later that for the slowest collisions for which the EC process is not negligible the CTMC calculations overestimate the direct ionization probabilities by about 30%. If the values for the electron capture are also overestimated by the CTMC model, the p_L^{DI} results obtained with our method would be as a consequence somewhat too small. It was however, estimated that a similar error of 30% in the CTMC EC values would change the obtained direct ionization probabilities by less than 4%.

Among the theories which describe ionization by charged projectiles and employ a quantum description of the atom, only the semiclassical approximation allows a detailed analysis of the ionization probabilities as a function of impact parameter. The SCA theoretical model was originally introduced by Bang and Hansteen [35]. SCA calculations are usually limited to the first-order time-dependent perturbation theory. In the present study we calculated the direct ionization probabilities according to the first-order SCA model of Trautmann and Rösel [23,24]. The latter employs classical hyperbolic trajectories and uses hydrogenlike Dirac electron wave functions. The effective charge of the target atom was calculated according to the method of Slater to account for screening effects. Binding energies of the separated atom model were employed. Multipoles up to the order $l = 5$ were considered in the calculations. The results of these SCA calculations are compared to the experimental direct ionization probabilities obtained in the present work in Fig. 6(a). First-order ionization models (including the SCA) predict that the ionization probability for a single L-shell electron increases as a function of the square of the projectile charge. For heavy-ion collisions the calculated probabilities may thus exceed unity. This indicates that the first-order approximation is no longer justified. The breakdown of the first-order SCA can be well seen in Fig. 6(a), which shows, in particular, that for low-energy collisions the variation of the direct ionization probabilities as a function of the projectile velocity depends on the ion type. At low velocities, where the probabilities are high (see Table IV), the ratio of the SCA and experimental probabilities clearly increases with the projectile charge. At high velocities, the ratios merge and converge to approximately 0.6 for the three different ions. Although first-order theories may also break down at higher velocities (see Ref. [36], and references therein) it seems that in our case the SCA model works rather well in this regime where the velocity dependence of the ionization probabilities is indeed quite well reproduced by our results. Furthermore, it may be expected that the remaining differences between the experimental and calculated direct ionization probabilities would be reduced by the use of better (Hartree-Fock) electron wave functions in the SCA calculations [10,37,38].

The geometrical model (GM) of Sulik *et al.* [39] can also provide direct ionization probabilities at zero impact parameter. In this model, which is based on the binary encounter approximation, the mean ionization probability for a single

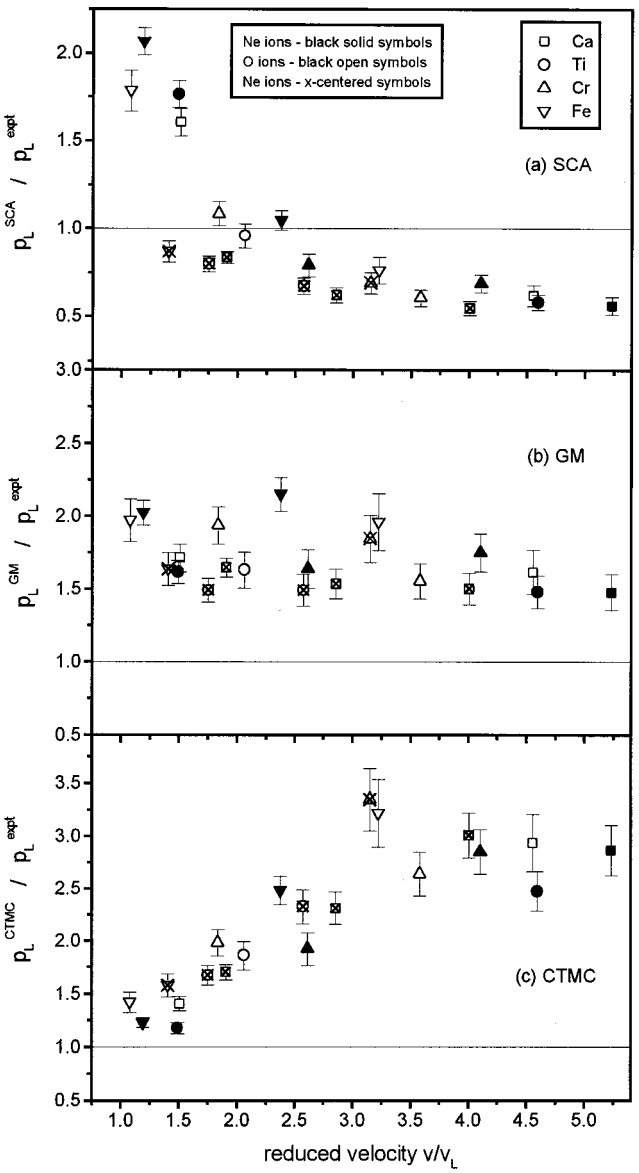

FIG. 6. Ratio of the theoretical to experimental direct ionization probabilities for a single L-shell electron as a function of the reduced projectile velocity. The comparison is presented for (a) the SCA model using hydrogenic wave functions [23,24], (b) the geometrical model [39], and (c) the three-body classical trajectory Monte Carlo model.

L-shell electron varies also with the square of the projectile charge. However, in contrast to the SCA model, GM direct ionization probabilities remain below unity for arbitrarily high projectile charges, at least for projectile velocities higher than the atomic orbital velocities. In the GM approach we consider a projectile at a velocity higher than the orbital electron velocity, passing through the target atom along a straight line at zero impact parameter. In the binary encounter the energy transferred to the target electron is a unique function of the projectile-electron impact parameter. Therefore, we can define a cylinder around the projectile trajectory in which the target electron acquires the amount of energy needed for ionization. The probability of ionization is then

given as the charge density fraction of one electron cut out by the cylinder. Using the hydrogenic single electron density distribution results in a scaling rule for the ionization probability at zero impact parameter, which tends to unify for high projectile atomic numbers in the high velocity limit [36]. The *L*-shell direct ionization probabilities of interest were also computed with the geometrical model. The results of these calculations are compared to our experimental data in Fig. 6(b). The comparison shows that the geometrical model describes reasonably well the velocity dependence of the experimental probabilities, although it overestimates the experimental values by approximately 80%. The differences can be assigned partly to the fact that this model yields values for the zero impact parameter, while our results correspond to an effective impact parameter of about 4000 fm.

Besides the electron capture probabilities which were used to fit the KL^N vacancy yields, the three-body CTMC model can also be employed to compute direct ionization probabilities. CTMC predictions for the direct ionization probabilities are presented in Fig. 6(c). It is found that CTMC calculations overestimate the experimental values. The differences increase with the reduced projectile velocity and start to level out at high velocities, where the ratio of the CTMC and experimental values tends to approximately 3.

V. CONCLUSION

The KL^N satellite x-ray spectra induced in Ca, Ti, Cr, and Fe targets by bombardment with 34-MeV C^{2+}, 72-MeV C^{3+}, and 134-MeV C^{4+} ions, 28-MeV O^{2+}, 64-MeV O^{3+}, and 230-MeV O^{6+} ions, and 43-MeV Ne^{3+}, 160-MeV Ne^{6+}, and 380-MeV Ne^{8+} ions were measured by means of a high-resolution von Hamos Bragg crystal spectrometer. From the intensity distributions of the resolved satellite lines the initial KL^N vacancy yields were deduced taking into account the atomic rearrangement processes preceding the *K* x-ray emission and the changes in the *K*-shell satellite fluorescence yields resulting from the additional inner-shell vacancies. The direct *L*-shell ionization probabilities per electron could then be determined by fitting these initial KL^N vacancy yields with a distribution, taking into consideration the direct ionization and electron capture contributions. The experimental ionization probabilities were compared to theoretical predictions obtained from the SCA, GM, and CTMC models. Comparison with the SCA calculations shows that for ion collisions with low-*Z* atoms, first-order theories break down at projectile velocities around matching condition for the *L*-shell electron, though they provide a satisfactory description of the ionization process in the high-velocity regime. The remaining differences between the experimental and calculated values in this high-velocity regime may be explained by the use of inappropriate hydrogenic wave functions in the SCA calculations. Geometrical as well as the CTMC models overestimate the experimental results. The geometrical model, however, describes the velocity dependence quite well, and yields results which are closer to the experimental values than those obtained in the CTMC approach. Furthermore, it was found that the differences between CTMC predictions and our experimental probabilities increase with the projectile reduced velocity up to about $\eta = 3$. In the high-velocity regime the ratios between CTMC theoretical predictions and the experimental values stabilize approximately at a factor of 3.

Finally we would like to point out that, as shown by the present study, reliable direct ionization probabilities can be extracted from the analysis of high-resolution x-ray satellite spectra, provided that the different ionization mechanisms that contribute to the observed KL^N satellite distributions are considered in detail, both theoretically and experimentally.

ACKNOWLEDGMENTS

The authors wish to thank Dr. Schmelzbach and the PSI Philips cyclotron crew for providing very good beam conditions. They also gratefully acknowledge the help of O. Mauron for the reflectivity measurements of the LiF(200) crystal. This work was mainly supported by the Slovenian Ministry of Science and Technology (Project No. J1-7473) and by the Swiss National Science Foundation. One of us (K.T.) also acknowledges support from OTKA (Grant No. T032306).

[1] R. L. Kauffman, J. H. McGuire, and P. Richard, Phys. Rev. A **3**, 1233 (1973).

[2] T. K. Li, R. L. Watson, and J. S. Hansen, Phys. Rev. A **3**, 1258 (1973).

[3] R. L. Watson, F. E. Jenson, and T. Chiao, Phys. Rev. A **4**, 1230 (1974).

[4] V. Dutkiewitcz, H. Bakhru, and N. Cue, Phys. Rev. A **1**, 306 (1976).

[5] K. W. Hill, B. L. Doyle, S. M. Shafroth, D. H. Madison, and R. D. Deslattes, Phys. Rev. A **4**, 1334 (1976).

[6] R. L. Watson, B. I. Sonobe, J. A. Demarest, and A. Langenberg, Phys. Rev. A **4**, 1529 (1979).

[7] B. Perny, J.-Cl. Dousse, M. Gasser, J. Kern, Ch. Rhême, P. Rymuza, and Z. Sujkowski, Phys. Rev. A **5**, 2120 (1987).

[8] P. Rymuza, Z. Sujkowski, M. Carlen, J.-Cl. Dousse, M. Gasser, J. Kern, B. Perny, and Ch. Rhême, Z. Phys. D: At., Mol. Clusters **14**, 37 (1989).

[9] P. Rymuza, T. Ludziejewski, Z. Sujkowski, M. Carlen, J.-Cl. Dousse, M. Gasser, J. Kern, and Ch. Rhême, Z. Phys. D: At., Mol. Clusters **23**, 71 (1992).

[10] B. Boschung, M. W. Carlen, J.-Cl. Dousse, B. Galley, Ch. Herren, J. Hoszowska, J. Kern, Ch. Rhême, T. Ludziejewski, P. Rymuza, Z. Sujkowski, and Z. Halabuka, Phys. Rev. A **5**, 3889 (1995).

[11] D. F. Anagnostopoulos, G. L. Borchert, and D. Gotta, J. Phys. B **25**, 2771 (1992).

[12] J. Hoszowska, J.-Cl. Dousse, J. Kern, Ch. Rhême, Nucl. Instrum. Methods Phys. Res. A **376**, 129 (1996).

[13] E. Storm, and H. I. Israel, Nucl. Data, Sect. A **7**, 565 (1970).

[14] M. Sanchez del Rio and R. J. Desus, Proc. SPIE **3152**, 148 (1997).

[15] R. J. Desus and M. Sanchez del Rio, Rev. Sci. Instrum. **67**, 3356 (1996).
[16] K. G. Dyall, I. P. Grant, C. T. Johnson, F. A. Parpia, and E. P. Plummer, Comput. Phys. Commun. **55**, 425 (1989).
[17] J. Végh, EWA, in *Proceedings of the Sixth European Conference on Applications of Surface and Interface Analysis, Montreaux, 1995*, edited by H. J. Mathieu, B. Reihl, and D. Briggs (Wiley, Chicester, 1996), pp. 679–682.
[18] F. P. Larkins, J. Phys. B **4**, L29 (1971).
[19] J. H. Scofield, At. Data Nucl. Data Tables **14**, 121 (1974).
[20] V. O. Kostroun, M. H. Chen, and B. Crasseman, Phys. Rev. A **3**, 533 (1971).
[21] M. O. Krause, J. Phys. Chem. Ref. Data **8**, 307 (1979).
[22] M. O. Krause and J. H. Oliver, J. Phys. Chem. Ref. Data **8**, 329 (1979).
[23] D. Trautmann and F. Rösel, Nucl. Instrum. Methods **169**, 259 (1980).
[24] D. Trautmann and F. Rösel, Nucl. Instrum. Methods Phys. Res. **214**, 21 (1983).
[25] T. W. Tunnel and C. P. Bhalla, Phys. Lett. A **86**, 13 (1981).
[26] K. Shima, T. Mikumo, and H. Tawara, At. Data Nucl. Data Tables **34**, 357 (1986).
[27] E. Träbert, P. Beiersdorfer, G. V. Brown, A. J. Smith, S. B. Utter, M. F. Gu, and D. W. Savin, Phys. Rev. A **3**, 2034 (1999).
[28] B. J. Wargelin, P. Beiersdorfer, and S. M. Kahn, Phys. Rev. Lett. **14**, 2196 (1993).
[29] R. W. Dunford, D. A. Church, C. J. Liu, H. G. Berry, M. L. A. Raphaelian, M. Haas, and L. J. Curtis, Phys. Rev. A **7**, 4109 (1990).
[30] A. E. S. Green, Adv. Quantum Chem. **7**, 221 (1973).
[31] K. Tokesi and G. Hock, J. Phys. B **29**, L119 (1996).
[32] B. Sulik, K. Tokesi, Y. Awaya, T. Kambara, and Y. Kanai, Nucl. Instrum. Methods Phys. Res. B **154**, 286 (1999).
[33] C. O. Reinhold and C. A. Falcon, Phys. Rev. A **33**, 3859 (1986).
[34] P. R. Bevington, *Data Reduction and Error Analysis for the Physical Sciences* (McGraw-Hill, New York, 1969), pp. 155 and 205.
[35] J. Bang and J. M. Hansteen, K. Dan. Vidensk. Selsk. Mat. Fys. Medd. **31** (13), 1 (1959).
[36] B. Sulik, G. Hock, and D. Berényi, J. Phys. B **17**, 3239 (1984).
[37] M. Kavčič, Ž. Šmit, M. Budnar, and Z. Halabuka, Phys. Rev. A **6**, 4675 (1997).
[38] Z. Halabuka, W. Perger and D. Trautmann, J. Phys. B **28**, 83 (1995).
[39] B. Sulik, I. Kádár, S. Ricz, D. Varga, J. Végh, G. Hock, and D. Berényi, Nucl. Instrum. Methods Phys. Res. B **28**, 509 (1983).